Three-axis torque investigation of interfacial exchange coupling in a NiFe/CoO bilayer micromagnetic disk: Supplementary Material

M.G. Dunsmore, J.A. Thibault, K.R. Fast, V.T.K. Sauer,
J.E. Losby, Z.Diao, M. Belov, and M.R. Freeman

(Dated: 28 January, 2022)

S1 Sample Fabrication

Primary considerations for the resonator design are paddle size, mechanical constants of the torsion arms, resonant frequency, torque sensitivity, and depth of undercut that forms a Fabry-Perot optical cavity between the resonator and the substrate base. Two sets of samples were fabricated. Each set has 120 samples that are organized into 6 arrays with 20 samples in each array.

The magnetic bilayers were patterned into discs having a diameter of 1.36 μm by electron beam lithography and lift-off. The magnetic thin film deposition was done using a confocal magnetron sputtering system (ATC Orion 8, AJA International) with 2-inch diameter targets (Plasmaterials, Inc.) The chamber base pressure was below 0.2 microTorr. The first layer, in contact with the resonator paddle, is antiferromagnetic cobalt oxide that was reactively sputtered from a cobalt target (deposition rate of 0.228 nm/min using RF power 118 W, sputtering gas pressure 4 mTorr, flow rates of 14 SCCM Ar and 6 SCCM O_2). Before depositing the ferromagnetic permalloy layer, the sputtering chamber was purged of oxygen by pressure cycling with argon (filling to argon pressure of 40 mTorr, holding for 60 seconds and then pumping down for 60 seconds, all repeated five times). The argon purge ensures that an antiferromagnetic oxide does not form on the surface of the FM layer (torque effects of NiO on permalloy were discovered by Prosen et al. in the early 1960s[1]). The permalloy layer was deposited on top of the cobalt oxide layer by DC sputtering from nickel and iron targets (40 W and 13 W powers, respectively, yielding deposition rates of 1.13 nm/min and 0.31 nm/min at 4 mTorr with a 20 SCCM argon gas flow rate). Both layers are 20 nm thick. The densities were assumed to be: 6.44 g/cm^3 for the cobalt oxide, 8.91 g/cm^3 for the nickel, and 7.86 g/cm^3 for the iron. A quartz crystal monitor was used to determine the deposition rates.

S2 Measurement Apparatus

The apparatus was designed to investigate the magnetic properties of nanoscale samples. The primary components of the apparatus are a cryostat, cryogen and vacuum systems, DC magnet and positioning system, Gauss meter, He-Ne laser, steering optics, three-axis objective positioning stage, photoreceiver, High Frequency RF lock-in amplifier (Zurich Instruments HF2LI), RF amplifier, control computer, and power supplies. Coarse adjustment of the cryostat temperature is done by manual control of the helium flow valves. Fine ($\pm$ 0.05 K) temperature stabilization is provided by PID control of a heater that is mounted in the cryostat. The system will stabilize at any desired operating point from helium temperature to 300 K. The apparatus is assembled on a standard optics table and is housed in an enclosure that provides stability of the ambient temperature.

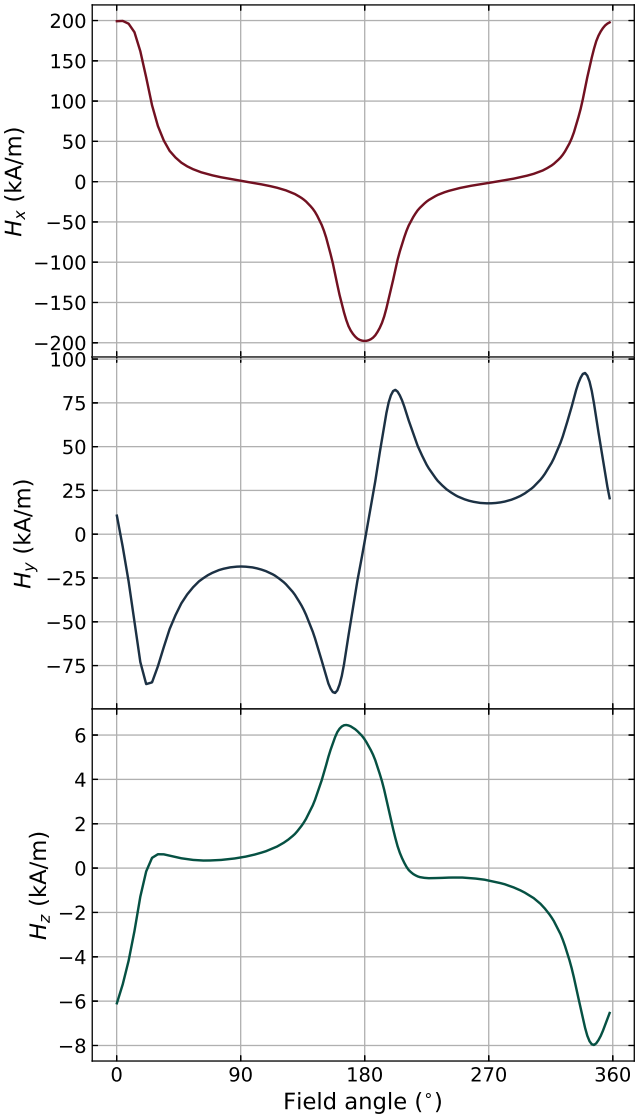

FIG. S1. The vector DC magnetic field calibration at the bias magnet position used for the measurements of Figs. 2, 3, and 4, plotted against in-plane field angle.

A. DC Field

A NdFeB permanent magnet (N42 alloy, 6" $\times$ 2" $\times$ 2" rectangular prism) is used for applying the DC bias magnetic

field. This choice is dictated by the need to avoid a proximal source of variable heat (as would be generated by an electromagnet) in order to maintain temperature stability of the apparatus. The permanent magnet has sufficiently strong external fields to suit a variety of applications: setting exchange bias, fixed field direction hysteresis measurements (with just a small window of inaccessible fields near zero bias), and rotational measurements where the in-plane field direction rotates through 360 degrees. The drawback of this approach is that the in-plane field magnitude does not remain constant as the magnet rotates. The magnet is rectangular thus causing the field strength variation to become larger as the centre of the magnet moves closer to the sample. The maximum and minimum in-plane fields were 199.8 kA/m at 359.6° and 17.7 kA/m at 93° respectively. A detailed field calibration was performed using a Hall probe at the sample position to measure each component of magnetic field during magnet rotations and translations such as are executed during the experimental measurements. The results of the calibration for the field rotation measurements are shown in Figure S1. Macrospin simulations of field rotations were conducted using an interpolated version of the field calibration data to ensure that the simulations reflected experimental conditions as closely as possible.

B. RF Field

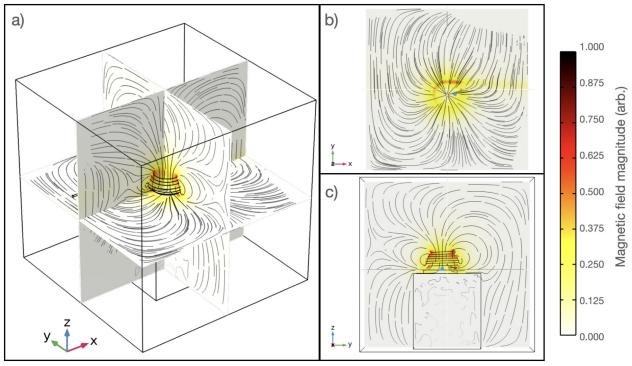

FIG. S2. COMSOL[2] simulations of RF field. There is a significant effect of screening that occurs due to the position of the silicon sample chips placement upon the cryostat cold finger. In panels b) and c), a blue dot is used to signify the approximate position of the sample beneath the coil.

Another matter of concern for three axis measurements of torque is the RF field strength along each Cartesian axis. The driving field in this case is generated by a hand-wound air core RF coil suspended above the sample. The coil winding was not uniform. The devices were offset from the coil axis, so as to produce a nonuniform field for driving multiple torque axes. As Figure S2 indicates, the driving field was strongest along the z and x direction and a very small driving field was expected along y. We modeled the coil using AutoDesk™Inventor and COMSOL's[2] Live Link feature. We simulated the field strength at a location corresponding to the sample position. Images of the sample and coil assembly were used to obtain the coil dimensions, relative position of the sample, and to bracket uncertainty in sample position. The results of the COMSOL study revealed the relative field strengths per Ampere of current. The field strengths were $H_x^{\mathrm{RF}} = (270 \pm 20)$ (A/m)/A, $H_y^{\mathrm{RF}} = (0 \pm 20)$ (A/m)/A, and $H_z^{\mathrm{RF}} = (350 \pm 20)$ (A/m)/A. The results of the simulation are shown in Figure S2. The blue dots in panels b) and c) represent the relative position of the sample beneath the coil. The simulated driving field strengths were used for calculating the three torque components.

C. Torque Generation

The DC bias field and RF dither fields combine in cross-products of the moments and external fields as follows,

$$\tau = \mu_0 \mathbf{m} \times \mathbf{H} \tag{1}$$

The individual torque components are,

$$\tau_x = \mu_0(m_y H_z - m_z H_y) \tag{2}$$
$$\tau_y = -\mu_0(m_x H_z - m_z H_x) \tag{3}$$
$$\tau_z = \mu_0(m_x H_y - m_y H_x) \tag{4}$$

The moments and fields have DC and RF components. Looking at τ_y, we can expand (3) to obtain,

$$\begin{aligned}\tau_y = -\mu_0[&(m_x^{DC} + m_x^{RF})(H_z^{DC} + H_z^{RF}) \\ &- (m_z^{DC} + m_z^{RF})(H_x^{DC} + H_x^{RF})]\end{aligned} \tag{5}$$

Grouping terms,

$$\begin{aligned}\tau_y = -\mu_0(&m_x^{DC} H_z^{DC} + m_x^{DC} H_z^{RF} \\ &+ m_x^{RF} H_z^{DC} + m_x^{RF} H_z^{RF} \\ &- m_z^{DC} H_x^{DC} - m_z^{DC} H_x^{RF} \\ &- m_z^{RF} H_x^{DC} - m_z^{RF} H_x^{RF})\end{aligned} \tag{6}$$

The lock-in amplifier only measures the component at the drive frequency. This leaves

$$\begin{aligned}\tau_y = -\mu_0(&m_x^{DC} H_z^{RF} + m_x^{RF} H_z^{DC} \\ &- m_z^{DC} H_x^{RF} - m_z^{RF} H_x^{DC})\end{aligned} \tag{7}$$

At saturation for the y-torque, the z-moment can be described by the susceptibility, while the x-moment is saturated thus substantially reducing its dependence on susceptibility and field. This yields a new form of the y-torque,

$$\begin{aligned}\tau_y = -\mu_0[&m_x^{DC} H_z^{RF} + m_x^{RF} H_z^{DC} \\ &- \chi_z V H_z^{DC} H_x^{RF} - \chi_z V H_z^{RF} H_x^{DC}]\end{aligned} \tag{8}$$

where the susceptibility χ_z is given as

$$\chi_z = \frac{M_s}{H_{x,\mathrm{eff}} + H_{x,\mathrm{appl}}} \tag{9}$$

with the effective field defined by the demagnetizing factors, $H_{\mathrm{eff}} = (N_z - N_r)M_s$. Equation 8 can be generalized to all torque axes.

S3 Thermomechanical Calibration

The thermomechanical calibration enables an absolute scale to be applied to the magnetically-driven mechanical torques and, in the present work, must be performed for three torsion axes. The calibration procedure is the same for each axis. The average potential energy of a torsion spring is given by,

$$\langle U \rangle = \frac{1}{2}\kappa_i^{\text{eff}}\langle\theta_i^2\rangle, \tag{10}$$

where κ_i^{eff} is the effective torsional spring constant for torsion axis i, and $\langle\theta_i^2\rangle$ is the average angle squared for an induced torque along the axis $i = (x, y, z)$. Utilizing the harmonic relation between angular frequency, moment of inertia and the effective spring constant, we used finite element analysis software[2] to model our device and perform an integration over the entire sample volume to obtain the moment of inertia for a given mode.

In the absence of an alternating magnetic field, the torque on the device is due to random thermal fluctuations, the frequency-independence of Brownian motion providing a broadband drive[3]. We use the equipartition of energy to equate the rotational energy and the thermal energy at temperature T. From this we find,

$$\langle\theta_i^2\rangle = \frac{k_B T}{\kappa_i^{\text{eff}}}, \tag{11}$$

where k_B is Boltzmann's constant. Under the assumption of small angles, we may modify the above equation to give the mean displacement by utilizing the distance from the axis of torque to the location of detection, $\langle x_i^2\rangle = R_i^2\langle\theta_i^2\rangle$. The mechanical response to such a thermal drive is described by a Lorentzian from which the frequency dependent angular spectral density, $S_{\theta_i}(f)$, can be obtained in units of rad^2/Hz for a mechanical device with torsional eigenfrequency f_i and quality factor Q_i,

$$S_{\theta_i\theta_i}(f) = \frac{2k_B T f_i^3}{\pi\kappa_i^{\text{eff}} Q_i}\frac{1}{(f_i^2 - f^2)^2 + (\frac{f f_i}{Q_i})^2}. \tag{12}$$

We may substitute (11) into this equation, and by taking the peak spectral density ($S_{\theta_i\theta_i}$ is maximized for $f = f_i$) and multiplying by R_i^2 we find the position spectral density, $S_{x_i x_i}$,

$$S_{x_i x_i} = \frac{2Q_i\langle x_i^2\rangle}{\pi f_i}. \tag{13}$$

From this equation, the thermomechanical torque spectral density is obtained using $\langle\tau_i\rangle = \kappa_i^{\text{eff}}\langle\theta_i\rangle$ and also scaling by Q_i^{-1} to account for the enhancement of displacement on mechanical resonance,

$$S_{\tau_i} = \frac{\kappa_i^{\text{eff}}\sqrt{\langle x_i^2\rangle}}{R_i Q_i}. \tag{14}$$

Finally, an analysis was performed to find the voltage spectral density from measured data $S_{V_iV_i}$ (temporal), corresponding to the square of the peak height minus the square of the technical noise floor, divided by the bandwidth of the lock-in measurement,

$$S_{V_iV_i} = \frac{V_{i,\text{peak}}^2 - V_{i,\text{background}}^2}{f_{\text{BW}}}. \tag{15}$$

The calibration factors, C_{τ_i}, were obtained by dividing the torque spectral densities by the square roots of the voltage spectral densities. The resulting factors are in units of Nm/V. In Table S1, the calibration constants are presented using the more natural scale of aNm/mV for the present measurements. The uncertainty in the thermomechanical calibration, resulting from an inadequate signal to noise ratio of required thermomechanical data near the apparatus noise floor, prevented any significant reduction in the overall uncertainty in the measurements. The second largest source of uncertainty was the RF field magnitude as mentioned in Section S2 B. The combination of these uncertainties results in a 20% systematic uncertainty in calibrated values of torque.

C_{τ_i}	Conversion at 295 K (aNm/mV)	Conversion at 69 K (aNm/mV)
C_{τ_x}	8.6±0.4	2.67±0.05
C_{τ_y}	5.0±0.5	2.90±0.09
C_{τ_z}	11.1±0.6	6.4±0.4

TABLE S1. Torque calibration constants obtained for the sample at ambient and cryogenic temperatures.

S4 In-plane torque at low bias field

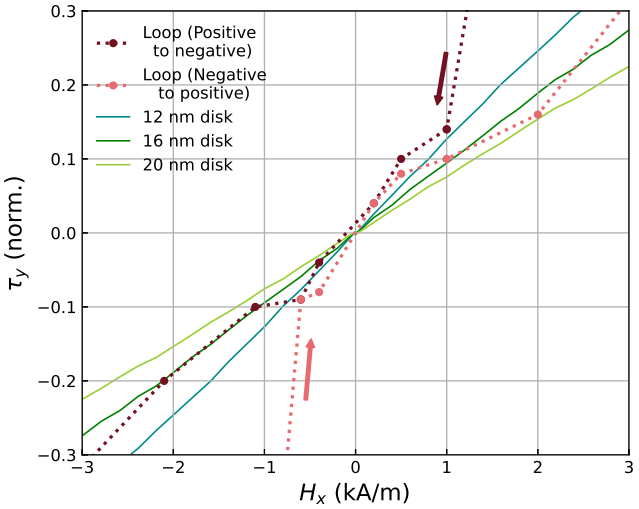

FIG. S3. In low external field strengths at room temperature, the permalloy disk demagnetizes, adopting a vortex spin texture. The experimental signature of vortex nucleation is indicated in the above plot by arrows. Mumax3 micromagnetic software[4] was used to simulate the vortex behaviour, and the results served to bracket the uncertainty in the magnetically active volume of the disk.

At room temperature in low bias field, and owing to constraints on the size of our magnetic sample, the permalloy

disk demagnetized to form a vortex spin texture. Details of the vortex state in this particular magnetic sample at room temperature have been previously discussed[5]. Experimental data of linear hysteresis loops, as shown in Figure S3, revealed the field where the vortex spin texture nucleated at sufficiently low bias field strength. Figure S3 shows the lowest field regime of a linear hysteresis loop. The experimental data is represented by solid points that are connected by dotted lines as a guide to the eye. The arrows next to the lines show the field sweep direction, and the section of line they are next to represents the irreversible decrease in y torque that marked the field where vortex nucleation occurred. The in-plane torque in low field followed a linear trend with occasional discrete steps due to the Barkhausen effect, related to the polycrystallinity of the sample[5]. The slope of this linear trend depends greatly on the ferromagnets aspect ratio since the only anisotropy present at room temperature is due to the shape of the magnetic sample. Three mumax3 micromagnetic simulations[4] were performed for comparison with data, and bracketed the uncertainty in the disk thickness. Performing these simulations with mumax3 was essential since it did not require a priori knowledge about the demagnetizing factors. The permalloy disk thickness was determined to be (16±1) nm.

We additionally used mumax3 simulations to ensure that the gyrotropic mode of the vortex state was sufficiently above the mechanical resonance, and that we could therefore assume a uniform susceptibility. Results from mumax3 gave a gyrotropic mode frequency of 100 MHz, well above the highest mechanical resonance frequency (4.23 MHz).

S5 In-plane torque at high bias fields and experimental justification for the macrospin description

In this section we describe how M_s was obtained from the field-dependence of the in-plane torque in magnetic saturation. Non-zero torques on specimens arise when there is an energy cost or gain from a magnetic moment rotating in response to a changing direction of applied field. If we describe a change in field direction by the addition of a small component, $\delta H_\perp$, perpendicular to an existing field, H_0, then in the complete absence of anisotropy the magnetic susceptibility, $\chi_\perp$, to $\delta H_\perp$ will be such that

$$\mu_0 m_0 \delta H_\perp - \mu_0 \chi_\perp \delta H_\perp H_0 = 0. \tag{16}$$

In other words, there is no torque perpendicular to the plane defined by m_0 (parallel to H_0 in the absence of anisotropy) and $\delta H_\perp$.

Qualitatively, the shape of the torque vs. applied field curves in Fig. 1 of the article is readily understood through the cross-products of magnetization and applied field. Strong shape anisotropy makes the out-of-plane $\chi_\perp$ small and nearly constant over this field range (in the thin disk limit, the out-of-plane demagnetization factor, N_z, is close to one), whereas the structure magnetizes much more easily in-plane . The out-of-plane susceptibility decreases significantly only for applied fields on the scale of the demagnetizing field, O(400 kA/m) in this case, when the Zeeman energy density becomes comparable. At low fields, the first term of equation 16 grows rapidly with H_0 while the second term remains small. At higher fields, after m_0 saturates, the second term continues to increase in magnitude as H_0 rises, causing the net torque to decrease. $\chi_\perp$ depends only on the demagnetization factors and saturation magnetization, M_s. The shape of the specimen is known from the nanofabrication steps and therefore M_s can be deduced from the measured curves. We extract M_s from comparisons with micromagnetic simulations[4] of torque thus avoiding the use of approximations such as the assumption of constant $\chi_\perp$.

In addition, we neglect the possibility of uniaxial perpendicular anisotropy affecting the determination of M_s because our samples are cooled with the fields applied in-plane. PMA in perpendicular field-cooled permalloy/CoO thin films is discussed by Zhou *et al.*[6] Scaling from the maximum positive interface anisotropy of 0.4 mJ/m^2 induced by Zhou *et al.* by cooling CoO/Py multilayers in perpendicular fields of 1.6 MA/m, to our samples if hypothetically cooled in strong perpendicular field, still leaves the high-field slope of the in-plane torque curve heavily dominated by the shape anisotropy but would require a 2% correction to our determination of M_s at liquid nitrogen temperatures. Micromagnetic simulations show that a positive PMA of 13 kJ/m^3 would, if neglected, cause a 2% underestimate of M_s.

In principle, there is redundancy inherent in this determination since the overall torque magnitude is also proportional to M_s. However, for the present experiment the combined uncertainties in thermomechanically-calibrated torque sensitivity and in RF drive field strength at the sample position make the torque magnitude determination of M_s less accurate than the high-field slope analysis, which gave values of (763±7) kA/m at 295 K and (801±8) kA/m at 68 K.

After the high-field torque slopes are established, it is straightforward to convert the measured x- and y-torques into y- and x-magnetic moments, respectively. The sums of the squares of the in-plane moments then yields a check on the constancy of the magnetic moment during field rotation. The results for the room temperature and $T = 68\,\mathrm{K}$ data from Fig. 2 are shown in Figure S4.

S6 LLG macrospin simulations

A. The LLG equation

We employ the continuum approximation for cases in which atomistic models cannot predict effects of condensed matter systems. In this regime, the magnetic moments of atoms within a condensed matter system are averaged, and their contributions to magnetization are treated classically. The Landau-Lifshitz-Gilbert equation is a differential equation that describes magnetization dynamics within the continuum approximation. The dynamical equation is as follows,

$$\frac{d\vec{M}}{dt} = -\gamma \vec{M} \times \vec{B}_{\mathrm{eff}} + \frac{\alpha}{M_S} \vec{M} \times \frac{d\vec{M}}{dt}, \tag{17}$$

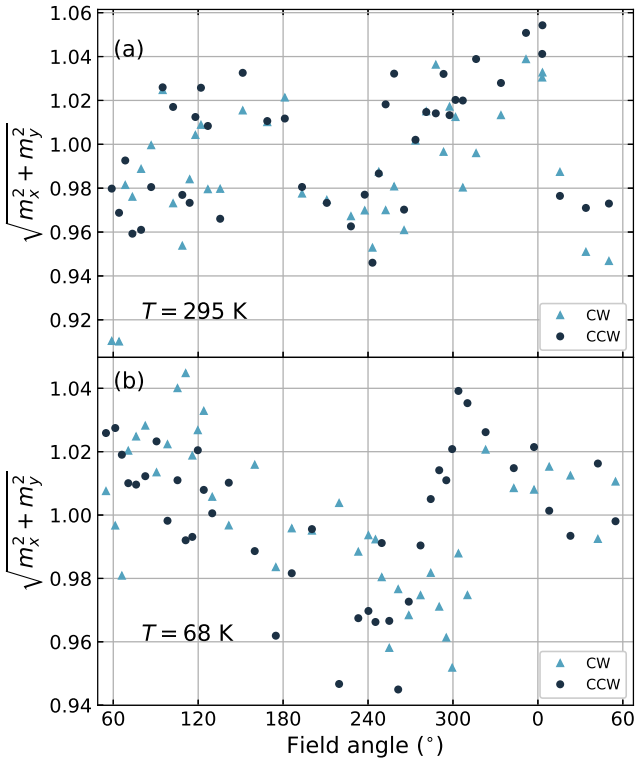

FIG. S4. Quadrature addition of magnetic moment components reveals that addition of the in plane magnetic moment components results in near unity for all angles at both ambient (a) and cryogenic (b) temperatures.

where $\vec{M}$ is the magnetization, γ is the gyromagnetic ratio, $\vec{B}_{\text{eff}}$ is the effective field, α is the Gilbert damping term, and M_S is the saturation magnetization. The LLG equation contains two terms: a precession term (coefficent γ) and a damping term (coefficent α/M_S). If we assume spherical symmetry ($M_r = M_S$) and define the effective field as the functional derivative of energy density, (ε), by magnetization ($\vec{B}_{\text{eff}} = -\frac{\delta\varepsilon}{\delta\vec{M}}$), we can rewrite the equation as a coupled system of differential equations in terms of polar (ϕ) and azimuthal (θ) angles,

$$\begin{aligned}\frac{d\theta}{dt} &= -\frac{\gamma}{\mu_0 M_s(1+\alpha^2)}\left(\frac{1}{\sin(\theta)}\frac{\partial\varepsilon}{\partial\phi} + \alpha\frac{\partial\varepsilon}{\partial\theta}\right)\\ \frac{d\phi}{dt} &= \frac{\gamma}{\mu_0 M_s(1+\alpha^2)}\left(\frac{-\alpha}{\sin^2(\theta)}\frac{\partial\varepsilon}{\partial\phi} + \frac{1}{\sin(\theta)}\frac{\partial\varepsilon}{\partial\theta}\right).\end{aligned} \tag{18}$$

Under conditions of sufficiently long time scales, the damping term will dominate the precession term and the magnetization will approach equilibrium. Our experimental frequencies were in the range of several MHz, not fast enough to meet the timescales of even the slowest dynamics predicted by the LLG equation. As such, we obtained a solution to the LLG equation and recorded the magnetization direction as polar and azimuthal angles in the portion of the solution dominated by damping. To calculate the AC torque, a dither field was applied to the field direction. Most of the AC field was along the z and x directions, while the AC field along y was very small in comparison owing to the position of the single RF excitation coil. COMSOL[2] simulations of field strength at the sample location were further corroborated by expected locations of zero crossings in the rotating data from our room temperature study of permalloy. The externally applied AC magnetic field is increased in the z and x directions by a small amount to a maxima, then decreased below the initial field to a minima, and finally increased back to it's original applied field strength. Following the dither steps, the DC field is then stepped to the next field angle where the process begins again. For each dither point, the torque was calculated in the usual way, $\vec{\tau} = \mu_0\vec{m}\times\vec{H}_{\text{ext}}^{\text{DC}}$. A linear fit was then applied to the torque response. The AC torque can be deduced from the slope of the fit.

B. Rotatable anisotropy

For most anisotropies, calculation of torque is straightforward. All that is required is to specify the strength of the anisotropy (by way of some anisotropy constant) and the angle at which the anisotropy axis is directed. For the rotatable anisotropy, however, extra care must be taken. The existence of the rotatable anisotropy axis is due to the exchange coupled uncompensated spins at the FM/AFM interface[7,8]. The energy density is written in the following way,

$$\varepsilon_{\text{rot}} = -K_{\text{rot}}\hat{M}_{\text{FM}}\cdot\hat{M}_{\text{rot}}, \tag{19}$$

where K_{rot} is the rotatable anisotropy constant, $\hat{M}_{\text{FM}}$ is the unit vector of the FM magnetization, and $\hat{M}_{\text{rot}}$ is the average direction of the uncompensated spins. Since these spins are able to rotate, they will follow the magnetization as it rotates with the applied field direction, however they may deviate slightly. To account for deviation we introduced a relative angle $\Delta\Phi_{\text{rot}}$ that defines the relative angle between the FM magnetization direction and the interfacial spins. We can rewrite equation 19 as,

$$\varepsilon_{\text{rot}} = -K_{\text{rot}}\cos(\Delta\Phi_{\text{rot}}), \tag{20}$$

which produces an easy axis along the direction $\Delta\Phi_{\text{rot}}$. If we apply a small perturbation ($\Delta\alpha$) to the angle of the FM magnetization, we find,

$$\varepsilon_{\text{rot}} = -K_{\text{rot}}\cos(\Delta\Phi_{\text{rot}} - \Delta\alpha). \tag{21}$$

There is a nonzero curvature in the energy density that will contribute to the AC torque. As such, when the DC field is stepped, there is no contribution from the rotatable anisotropy, but on subsequent AC dither cycles, the rotatable anisotropy term is included and contributes to the torque.

C. Additional contributing anisotropies

Exchange coupling between FM and AF layers introduces rotatable, spin-flop and unidirectional anisotropy terms given by the following energy density equation

$$\begin{aligned}\varepsilon_{\text{A}} = &-K_{\text{SF}}\sin^2(\theta)\cos^2(\phi-\phi_{\text{SF}}) -\\ &K_{\text{EB}}\sin(\theta)\cos(\phi-\phi_{\text{EB}}) - K_{\text{rot}}\hat{m}_{\text{FM}}\cdot\hat{H}_{\text{rot}}.\end{aligned} \tag{22}$$

Aside from the rotatable anisotropy (described in subsection S6 B), implementation of spin-flop and unidirectional anisotropies is straightforward.

The shape anisotropy is obtained from equations derived by Joseph[9] to calculate the cylindrical demagnetization factors. The demagnetizing energy density is thus,

$$\varepsilon_{\mathrm{D}} = \frac{1}{2}\mu_0 M_S^2 \big(N_x \cos^2(\phi)\sin^2(\theta) + N_y \sin^2(\phi)\sin^2(\theta) + N_z \cos^2(\theta)\big) \tag{23}$$

where N_i is the demagnetizing factor along axis i. Finally we introduce the Zeeman energy density that describes the effect of an external field on the macrospin

$$\varepsilon_{\mathrm{Z}} = -\mu_0 \vec{m}_{\mathrm{FM}} \cdot \vec{H}_{\mathrm{ext}}^{\mathrm{DC}}. \tag{24}$$

D. Curve fitting

A unique match of the data to the multi-parameter model is possible because each anisotropy parameter affects specific features of the AC torque curve independent of the other anisotropies. We presume that the shape anisotropy is identical at both room temperature, and cryogenic temperatures. The demagnetizing energy density has a significant effect on the τ_x and τ_y curves, however since we are considering a cylindrical sample $N_x = N_y$, no τ_z signal is observed as a result of shape anisotropy. As a consequence, all components of the τ_z curve are derived from anisotropies that emerge due to exchange coupling between the FM and AF layers. We introduce three anisotropies that are a direct result of exchange coupling: the rotatable anisotropy that represents the effect due to exchange coupled compensated AF spins, unidirectional anisotropy that represents exchange bias, and uniaxial anisotropy that represents spin-flop. The rotatable anisotropy term produces the 1-fold rotational symmetry that is dominant in the low temperature τ_z data. The rotatable anisotropy magnitude accounts for the slope of the linear regions around the zero crossing. The unidirectional exchange bias anisotropy term, at the field cooling angle presented in Figure 3 of the manuscript, contributes an extrema height asymmetry. The angle that the unidirectional anisotropy is applied along can specifically suppress the height of one of the two extrema that come from the contribution of the rotatable anisotropy. Finally, the uniaxial anisotropy accounts for the contribution of canting spins in the AF layer (spin-flop), which reduces the magnitude of the peaks due to the rotatable anisotropy.

Fitting the low temperature z-torque data to the model yielded a minimum $\chi^2_{\nu,\mathrm{min}}$ value of 1.2 where χ^2_ν was calculated from

$$\chi^2_\nu = \frac{1}{\nu}\sum_i \frac{(\tau_i^{\mathrm{exp}} - \tau_i^{\mathrm{model}})^2}{(\delta\tau_i^{\mathrm{exp}})^2}, \tag{25}$$

where τ_i^{exp} is the value of the i-th data point, τ_i^{model} is the value of the i-th point of the macrospin solution, ν is the degrees of freedom (number of data points minus the number of fit parameters), and $\delta\tau_i^{\mathrm{exp}}$ is the uncertainty in the i-th data point. Each parameter is varied around its best-fit value to obtain $\chi^2_\nu + \delta\chi^2_\nu$ where $\delta\chi^2_\nu = \sqrt{2\nu}$. In the present work $\chi^2_{\nu,\mathrm{min}} = 1.2$ and $\delta\chi^2_\nu = 0.3$ so each parameter (K_{EB}, ϕ_{EB}, K_{SF}, ϕ_{SF}, K_{rot}, $\Delta\Phi_{\mathrm{rot}}$) is varied such that $\chi^2 = 1.5$, thus bracketing the 1 sigma confidence interval of each parameter individually. We find $K_{\mathrm{EB}} = (0.10 \pm 0.05)$ kJ/m^3, $\phi_{\mathrm{EB}} = 55^\circ \pm 3^\circ$, $K_{\mathrm{SF}} = (8.3 \pm 0.3)$ kJ/m^3, $\phi_{\mathrm{SF}} = -91^\circ \pm 2^\circ$, $K_{\mathrm{rot}} = (22 \pm 1)$ kJ/m^3, and $\Delta\Phi_{\mathrm{rot}} = -5^\circ \pm 3^\circ$.

E. Dynamics

Determination of magnetization dynamics is not the only way to study anisotropic systems, especially for long timescales without dynamics. An analysis was also performed by using the Stoner-Wohlfarth model in 2D to obtain the out of plane torque. Good agreement between Stoner-Wohlfarth and LLG simulation methodologies was observed. While 3 dimensional extensions of the Stoner-Wohlfarth model can also be used to model 3 axis torques, the LLG equation was used for analysis of high field hysteresis loops to bracket M_S and the magnetic aspect ratio. Further studies of micromagnetic exchange bias will undoubtedly benefit from LLG micromagnetic simulation[10–12]. Presenting a LLG macrospin model that agrees with models such as Stoner-Wohlfarth serves as an appropriate jumping off point for subsequent studies of micromagnetic exchange bias wherein micromagnetic domain structure plays an essential part.

[1] R. Prosen, J. Holmen, and B. Gran, "Rotatable anisotropy in thin permalloy films," Journal of Applied Physics **32**, S91–S92 (1961).

[2] "COMSOL Multiphysics (TM), v.5.6, www.comsol.com, COMSOL AB, Stockholm, Sweden.".

[3] J. Losby, J. A. Burgess, Z. Diao, D. C. Fortin, W. K. Hiebert, and M. R. Freeman, "Thermo-mechanical sensitivity calibration of nanotorsional magnetometers," Journal of Applied Physics **111**, 07D305 (2012).

[4] A. Vansteenkiste, J. Leliaert, M. Dvornik, M. Helsen, F. Garcia-Sanchez, and B. Van Waeyenberge, "The design and verification of mumax3," AIP Advances **4**, 107133 (2014).

[5] K. R. Fast, J. A. Thibault, V. T. K. Sauer, M. G. Dunsmore, A. Kav, J. E. Losby, Z. Diao, E. J. Luber, M. Belov, and M. R. Freeman, "Simultaneous three-axis torque measurements of micromagnetism," AIP Advances **11**, 015119 (2021).

[6] S. M. Zhou, L. Sun, P. C. Searson, and C. L. Chien, "Perpendicular exchange bias and magnetic anisotropy in CoO/permalloy multilayers," Physical Review B **69**, 024408 (2004).

[7] R. D. McMichael, M. D. Stiles, P. Chen, and W. F. Egelhoff Jr, "Ferromagnetic resonance studies of NiO-coupled thin films of $Ni_{80}Fe_{20}$," Physical Review B **58**, 8605 (1998).

[8] M. D. Stiles and R. D. McMichael, "Model for exchange bias in polycrystalline ferromagnet-antiferromagnet bilayers," Physical Review B **59**, 3722 (1999).

[9] R. I. Joseph, "Ballistic demagnetizing factor in uniformly magnetized cylinders," Journal of Applied Physics **37**, 4639–4643 (1966).

[10] J. De Clercq, A. Vansteenkiste, M. Abes, K. Temst, and B. Van Waeyenberge, "Modelling exchange bias with mumax3," Journal of Physics D: Applied Physics **49**, 435001 (2016).

[11] J. De Clercq, J. Leliaert, and B. Van Waeyenberge, "Modelling compensated antiferromagnetic interfaces with mumax3," Journal of Physics D: Applied Physics **50**, 425002 (2017).

[12] J. De Clercq, *Modelling antiferromagnetic interfaces with MuMax3*, Ph.D. thesis, Ghent University (2017).